

Kinematics of elliptical galaxies with a diffuse dust component { II. Dust effects on kinematic modelling

Marten Baes^{1,2}, Herwig Dejonghe¹ and Sven De Rijcke^{1,2}

¹Sterrenkundig Observatorium Universiteit Gent, Krijgslaan 281 S9, B-9000 Gent, Belgium

²Research Assistant of the Fund for Scientific Research - Flanders (Belgium)

20 May 2019

ABSTRACT

Observations have demonstrated the presence of substantial amounts of interstellar dust in elliptical galaxies, most of which is believed to be distributed diffusely over the galaxy. Absorption by dust grains has a major impact on the transfer of stellar radiation, and affects the projection of each physical (and kinematic) quantity. In a previous paper, we have investigated the effects of a diffusely distributed dust component on the observed kinematics of spherical galaxies. In this paper we investigate the effect of not taking dust into account in dynamical modelling procedures. We use a set of semi-analytical dusty galaxy models to create synthetic LOSVD data sets, which we then model as if no dust were present.

We find some considerable differences between the best-fitting models and the input models, and we find that these differences are dependent on the orbital structure of the input galaxy. For radial and isotropic models on the one hand, we find that the dynamical mass of the models decreases nearly linearly with optical depth, with an amount of 5 per cent per optical depth unit, whereas their orbital structure is hardly affected. For tangential models on the other hand, the dynamical mass decrease is smaller, but their orbital structure is affected: their distribution functions appears less tangentially anisotropic. For all models the mass-to-light ratio will be underestimated, by a factor of around 20 per cent per optical depth unit.

We discuss these results in the light of the limited effects of dust extinction on the LOSVDs, as obtained in paper I, and conclude that the determination of the dynamical mass and the kinematic structure of galaxies is not only determined by the observed kinematic quantities, but is also critically dependent on the potential and hence the observed light profile. We argue that dust, even in rather modest amounts, should therefore be taken into account in kinematic modelling procedures.

Key words: dust, extinction { galaxies : elliptical and lenticular, CD { galaxies : ISM { galaxies : kinematics and dynamics

1 INTRODUCTION

It has become well-established that early-type galaxies contain a considerable amount of interstellar dust. In the optical dust is detected in ellipticals by its obscuration effects on the light distribution, when it is present in the form of dust lanes and patches (e.g. Ebner & Balick 1985, Veron-Cetty & Veron 1988, van Dokkum & Franx 1995). In emission, dust is detected by the IRAS satellite in the 60 and 100 μ m wavebands (Knapp et al. 1989, Roberts et al. 1991). In a comparative analysis Goudfrooij & de Jong (1995, hereafter GdJ95) show that the dust masses derived from FIR data are about a factor of ten higher than those calculated from optical data. Using a more detailed dust mass estimator which includes a temperature distribution for the dust grains

(Kwan & Xie 1992), Merluzzi (1998) shows that GdJ95 still underestimated the FIR dust masses with a factor up to six. Also submillimeter observations (Fich & Hodge 1991, 1993, Wiklind & Henkel 1995) and ISO data beyond 100 μ m (Haas 1998), that may be able to detect the very cold dust for which IRAS is insensitive ($T < 25$ K), suggest that the dust masses could be up to an order of magnitude higher than observed from FIR observations alone.

This difference between the absorption and emission dust masses in elliptical galaxies is called the dust mass discrepancy. It cannot be solved by a more critical reconsideration of the IRAS data (Bregman et al. 1998), by corrections for the optical absorption in the dust lanes (Merluzzi 1998) or by taking into account the dust recently ejected from evolved stars (Tsai & Mathews 1996). The interstellar dust

medium in ellipticals hence has to be composed of (at least) two components: a lesser massive one which is optically visible in the form of dust lanes and patches, and a more massive one which is distributed over the galaxy and is hard to detect optically. The spatial distribution of this component is still unclear. GdJ95 suggest that it is distributed over the inner parts of the galaxy, which supports the evaporation flow scenario. In this picture, most of the gas and dust has an external origin: clouds of interstellar matter have been accreted during interactions/merging with a gas-rich galaxy, and they gradually evaporate in the hot X-ray emitting gas (Sparks, Machedetto & Golombek 1989, de Jong et al. 1990, Forbes 1991, GdJ95). Tsai & Mathews (1996) and Wise & Silva (1997) on the other hand suggest that dust is not connected to the inner few kpc only, but also extends to larger radii. Such a dust distribution supports a scenario where gas and dust have an internal origin: it can be associated with red giant winds or formed in connection with star formation in cooling flows (Fabian, Nulsen & Canizares 1991; Knapp, Gunn & Wynn-Williams 1992; Hansen, Jørgensen & Nørgaard-Nielsen 1995). However, none of these mechanisms seems to be able to explain the FIR observations satisfyingly, and a combination of both mechanisms may be at work (Merluzzi 1998). As in the first paper of this series (Baes & Dejonghe 2000, hereafter paper I), we will assume that dust is distributed smoothly over the entire galaxy.

Absorption by dust grains has a major impact on the transfer of stellar radiation through the interstellar medium. It therefore affects the projection, i.e. the integration along the line-of-sight (hereafter LOS) of the intrinsic three-dimensional light distribution. A number of studies have investigated the effects of a diffuse dust distribution upon the photometry of ellipticals (Witt, Thronson & Capuano 1992, GdJ95, Silva & Wise 1996, Wise & Silva 1996; hereafter WS96). But dust does not only affect the projection of the light distribution, it affects the projected kinematics too. This is of particular importance in stellar dynamics, where the ultimate purpose is the determination of the phase space distribution function $F(r;v)$, hereafter DF, describing the entire dynamical structure. This DF is usually constructed by fits to the LOSVDs or their moments, and hence it is obviously important to examine to which extent these are affected by dust obscuration.

In paper I we constructed a set of semi-analytical models in order to investigate the effects of dust absorption on the light profile, the projected velocity dispersion profile and the LOSVDs. Concerning the photometry, we find that diffuse dust has a strong impact: a global attenuation, strong extinction in the central regions, the formation of radial color gradients, and an increasing apparent core radius. In spite of the simplified character of our analysis (we don't include scattering effects in our models), these results are in qualitative correspondence with the conclusions of the more detailed photometric studies mentioned before. The effect of dust on the projected dispersion profile or the LOSVDs is of a totally different nature. The effects are a redistribution along the LOS: dust makes the contribution of the nearer parts more important, relative to the more distant parts. Therefore it is no big surprise that, in a spherically symmetric galaxy, the LOSVDs are quite insensitive to modest amounts of dust. For example, for a modest optical depth ($\tau = 2$) the effect on the projected velocity dispersion is

around 2 percent in the central regions. However, for higher optical depths, these effects do become considerable, which can be important on a local scale: e.g. asymmetries in the projected kinematics may be the result of a large extinction in a compact region, such as in the dust lane elliptical NGC 5266 (Mollenhof & Arenbach 1986). More details can be found in paper I.

The fact that both the photometry and the observed kinematics are affected by dust obscuration will have consequences on the dynamical modelling of galaxies. Now that we understand the way dust absorption affects the projected kinematics, it is obvious that dust needs to be accounted for in deprojection procedures, or more general, in kinematic modelling procedures. It is the scope of this paper to determine the effects of neglecting dust in the modelling of kinematic data. In other words, if one tries to model dust-augmented kinematic profiles without taking dust into account, as is usually done, to what extent are erroneous conclusions drawn about the kinematic structure of the galaxy? In order to answer this question we will create synthetic dust-augmented data sets, and model them as if no dust were present.

In section 2 and section 3 we describe the construction of the data sets and the modelling procedure. The results of the modelling are presented in section 4, and in section 5 we investigate whether these depend critically on the choice of the dust geometry. A discussion of the results is given in section 6.

2 THE DATA SETS

2.1 The model

To create our data sets, we construct a set of two-component galaxy models, consisting of a stellar and a dust component. Both components are spherically symmetric.

For the stellar component, we use a Plummer model (Dejonghe 1987), which is described by the potential-density pair

$$\Phi(r) = \frac{GM_0}{c} \left[1 + \frac{r^2}{c^2} \right]^{\frac{1}{2}} \quad (1a)$$

$$\rho(r) = \frac{3}{4} \frac{M_0}{c^3} \left[1 + \frac{r^2}{c^2} \right]^{-\frac{5}{2}}; \quad (1b)$$

with $c = 5$ kpc the so-called core radius and $M_0 = 5 \cdot 10^{10} M_\odot$ the total mass. Furthermore we assume a constant mass-to-light ratio $\Upsilon = 4$, such that the three-dimensional light distribution is given by $\rho(r) = \frac{1}{4} \rho(r)$.

With the technique described by Dejonghe (1986) one finds a family of two-integral DFs $F_q(E;L)$ that self-consistently generate the Plummer potential-density pair (1ab). This family has two interesting properties, which justify its choice as a generic model for the class of elliptical galaxies (although its projected density profile does not resemble elliptical galaxies). First, the models are completely analytical, i.e. the DF and all the (projected) moments can be calculated analytically. And second, the family depends on one single parameter q which can be varied continuously in order to obtain tangential ($q < 0$), isotropic ($q = 0$) or radial ($0 < q < 2$) models. We consider a set of different orbital structures, characterized by the parameters $q = 6, 2, 0$ and 1. In the sequel of this paper we will refer to them

Table 1. Some parameters of the dusty Plummer models as a function of the optical depth τ . The second column gives the observed core radius, the third and the fourth column give the observed luminosity and the total extinction, and column six and seven list the projected light density and projected dispersion for the central LOS. This dispersion is tabulated for the isotropic model, one finds the central dispersion of the very tangential, tangential and radial models by multiplying this with the factors $\beta_2=2$, $\beta_3=2$ and $\beta_6=5$ respectively.

	c_{obs} (kpc)	L_{obs} ($10^9 L_{\odot}$)	A (mag)	$\rho_{\text{p};0}$ (L_{\odot}/pc^2)	$\sigma_{\text{p};0}$ (km/s)
	0.0	5.00	12.50	0.00	159.2
	0.5	5.33	11.08	0.13	124.7
	1.0	5.65	9.91	0.25	99.0
	1.5	6.02	8.93	0.37	79.5
	2.0	6.35	8.11	0.47	64.6
	2.5	6.74	7.41	0.57	53.1
	3.0	7.15	6.81	0.66	44.2

as very tangential, tangential, isotropic and radial models respectively.

As in paper I, we only incorporate the effects of dust absorption and neglect scattering effects. Then, the dust component is completely determined by the opacity function $\kappa(r)$, for which we use a modified Hubble profile

$$\kappa(r) = \frac{1}{2c} \left(1 + \frac{r^2}{c^2} \right)^{-\frac{3}{2}} \quad (2)$$

The normalization is such that $\int_0^Z \kappa(r) ds$ equals the total optical depth, defined as the projection of the opacity along the entire central LOS²

$$\int_{\text{central LOS}} \kappa(r) ds = 2 \int_0^{Z+1} \kappa(r) dr \quad (3)$$

As W S96 and paper I, we take the same core radius for the dust and the stars; the choice of the opacity function is critically investigated in chapter 5. We only consider optical depths ranging from $\tau = 0$ to $\tau = 3$ in our calculations, as high values for the optical depth associated with a diffuse dust component seem not to be in accordance with photometric studies (G dJ95, W S96).

2.2 The projections

For each model we create a set of so-called dusty projected kinematic data. A dusty projected quantity $\rho_{\text{p}}(x;v)$ differs from a normal projected quantity as it is a weighted integral along the LOS x of a three-dimensional spherically symmetric quantity $\rho(r;v)$. We assume that the galaxy is located at a distance which is significantly larger than its size. Then the errors made by assuming parallel projection, which are of the order $(c/D)^2$ with D the distance to the galaxy, are negligible (see Paper I, section 2). For a dusty galaxy with opacity function $\kappa(r)$ the appropriate formula reads

$$\rho_{\text{p}}(x;v) = 2 \int_x^{Z+1} K(x;r) \frac{\rho(r;v) r dr}{r^2 x^2}; \quad (4a)$$

² Throughout paper I and this paper we use this definition of τ , whereas e.g. W S96 defined τ as the integral of the opacity from the centre of the galaxy to the edge, half our value.

where $K(x;r)$ is a weight function defined as

$$K(x;r) = \exp \left[-\frac{\int_x^{Z+1} \kappa(r) r dr}{r^2 x^2} \cosh \frac{Z-r}{x} \frac{\int_r^{Z+1} \kappa(r') r' dr'}{r'^2 x^2} \right]; \quad (4b)$$

Details can be found in section 2 of paper I. We substituted the analytical expressions for the moments of the DF, together with the opacity function (2), in expression (4a) to obtain dusty projected profiles, such as the projected light density $\rho_{\text{p}}(x)$ and the projected velocity dispersion $\sigma_{\text{p}}(x)$. Since in particular the projected light density will depend on the optical depth, we will have to be careful in our terminology when calculating quantities such as the luminosity and the core radius. We need to discriminate between true and observed quantities, which are respectively derived from the spatial and the projected distribution. For example, the true luminosity of the galaxy is calculated by integrating the light density over space

$$L = 4 \int_0^{Z+1} \rho(r) r^2 dr; \quad (5)$$

which is of course independent of the optical depth and equals $M_0 = 1.25 \cdot 10^{10} L_{\odot}$. The observed luminosity L_{obs} is calculated by integrating the projected light density over the plane of the sky,

$$L_{\text{obs}} = 2 \int_0^{Z+1} \rho_{\text{p}}(x) x dx; \quad (6)$$

and is a function of τ . Analogously, all our Plummer models have a (true) core radius $c = 5$ kpc, whereas their observed core radius c_{obs} will depend on the optical depth (see section 3.1). In table 1 we tabulate some of the parameters of our dusty Plummer models.

2.3 The data sets

Each data set consists of the projected light density data $\rho_{\text{p}}(x)$ and projected dispersion data $\sigma_{\text{p}}(x)$, which are taken at $x = 0$ kpc, 0.5 kpc, ..., 10 kpc. However, since dispersion profiles depend on both the orbital structure and the mass distribution, they do not sufficiently constrain the dynamical structure of the galaxy. This mass-anisotropy degeneracy can be broken by including the higher order Gauss-Hermite moments in the fitting routine (van der Marel & Franx 1993, Gerhard 1993). Since we work with simulated data, we are able to include LOSVD data points directly in the modelling procedure. We assume that these data are noiseless, such that our data set is perfect, i.e. it contains all the kinematic information that could be available from perfect observations. Altogether each data set consists of 252 data points.

3 THE MODELLING PROCEDURE

3.1 Determination of the potential

The first step in the modelling of kinematic data is the determination of the potential. Although we have a perfect data set at our disposal, we are not able to constrain the potential completely without any assumptions, not even in the case of spherical symmetry (Dejonghe & Merritt 1992).

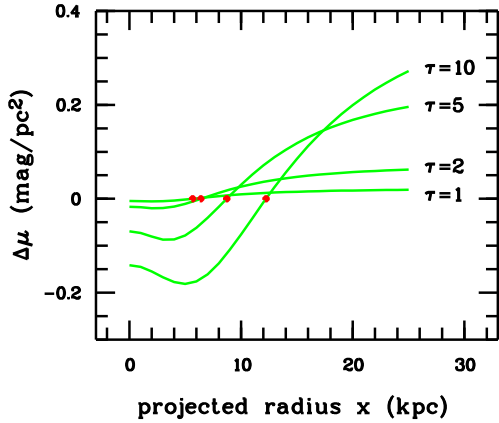


Figure 1. The difference $\Delta\mu(x)$ in surface brightness between our dusty projected density profiles and the best fitting Plummer light profiles, for the modest optical depths $\tau = 1$ and $\tau = 2$, and also for the higher values $\tau = 5$ and $\tau = 10$. It is clear that for modest optical depths a Plummer profile provides a satisfactory fit to the dust-augmented profiles, such that we can safely assume a Plummer potential in our modelling procedure. The dots in the figure indicate the observed core radii c_{obs} of the Plummer light profiles, where by construction $\nu_p(c_{\text{obs}}) = \nu_p^{-1}(c_{\text{obs}})$.

In this first approach we assume that it makes sense to consider a constant mass-to-light ratio, such that the spatial dependence of the potential can be derived from the projected light density $\nu_p(x)$. It can be calculated numerically for our set of models, but we prefer to work with a potential whose functional form is explicitly known. We find that, for the modest optical depths we are considering, the dust-augmented light profiles of our models can still be satisfyingly described by Plummer light profiles

$$\nu_p^{-1}(x) = \nu_{p,0} \left[1 + \frac{x^2}{c_{\text{obs}}^2} \right]^{-2}; \quad (7)$$

with c_{obs} dependent on the optical depth. In figure 1 we plot the difference

$$\Delta\mu(x) = 2.5 \log \frac{\nu_p(x)}{\nu_p^{-1}(x)}; \quad (8)$$

in surface brightness between the dusty projected light density profiles $\nu_p(x)$ and the best fitting Plummer light profiles $\nu_p^{-1}(x)$. Even at very large projected radii we find that never becomes larger than 0.05 for $\tau = 2$, such that we can say that the Plummer character of the galaxy is preserved for modest values of τ . We will therefore assume a Plummer potential

$$\nu(r) = \frac{GM}{c_{\text{obs}}} \left[1 + \frac{r^2}{c_{\text{obs}}^2} \right]^{-\frac{1}{2}} \quad (9)$$

for our models, with c_{obs} determined from the best fit to the $\nu_p(x)$ data, and the mass M still featuring as a free parameter. The values for c_{obs} are tabulated in the second column of table 1.

3.2 Determination of the DF

With a fixed potential there exists one and only one two-integral DF $F(E; L^2)$ that fits the kinematic data (Dejonghe

& Merritt 1992). It is always possible to write this DF as a finite sum of components

$$F(E; L^2) = \sum_{i=1}^N c_i F^i(E; L^2) \quad (10)$$

where c_i are the coefficients and the components $F^i(E; L^2)$ form a complete set of simple dynamical models. For any observed kinematic data point $n(x; v)$ the same expansion is valid,

$$n = \sum_{i=1}^N c_i \nu_n^i; \quad (11)$$

since these moments depend linearly on the DF. Practically one can only consider a finite number N of components,

$$F(E; L^2) = \sum_{i=1}^N c_i F^i(E; L^2); \quad (12)$$

The best fitting coefficients can then be found by minimizing a χ^2 -like variable

$$\chi^2 = \sum_n \frac{1}{w_n} \left[\sum_{i=1}^N c_i \nu_n^i - n \right]^2; \quad (13)$$

where the sum contains all data points, and w_n is the weight accorded to the n th data point. Since we assume to obtain perfect, noiseless synthetic data, we can use these weights to (arbitrarily) set the relative importance of each data point in the global χ^2 . For the projected density points we take $w_n = 1$, for the projected dispersion $w_n = \frac{1}{3}$ and for the LOSVD data the weight varies from $w_n = \frac{1}{3}$ at the centre to $w_n = \frac{1}{10}$ in the outer parts. This χ^2 is quadratic in the coefficients and has to be minimized under the linear constraint that the DF has to be positive over a grid $(E_j; L_k^2)$ in phase space,

$$\sum_{i=1}^N c_i F^i(E_j; L_k^2) \geq 0 \quad \text{for all } j \text{ and } k, \quad (14)$$

which amounts to a typical Quadratic Programming problem. For details we refer to Dejonghe (1989).

We choose our components from a library of Frick models. These are simple dynamical models that are defined by the augmented density²,

$$\nu(r) = a \frac{r^{2b}}{s}; \quad (15)$$

where s is a scale factor and a and b are real numbers that satisfy the condition $a - 2b > 3$ to keep the total mass finite. The anisotropy $\beta(r)$, generally defined as

$$\beta(r) = 1 - \frac{\sigma_r^2}{\sigma_\theta^2}; \quad (16)$$

will be constant for these models, since the r -dependence is a power law (Dejonghe 1986, section 1.5.1). We find immediately $\beta(r) = b$, hence the condition $b > 1$ is required. The

² The augmented density is the density written as a function of the radius r and the potential ν . It is a fundamental quantity in a technique to construct 2-integral distribution functions (Dejonghe 1986).

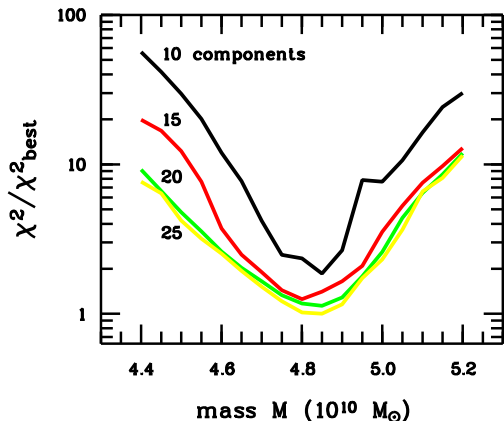


Figure 2. Plot showing χ^2 as a function of the mass M , for a tangential input model with $\beta = 1$. The χ^2 values have no absolute meaning. The dynamical mass is determined at the minimum of the plot, being $4.85 \times 10^{10} M_{\odot}$. The plot is shown for models containing 10, 15, 20 and 25 components. Clearly 20 components are sufficient to determine the dynamical mass accurately.

two-integral DF corresponding to (15) is a simple power-law of E and L^2

$$F(E; L^2) / E^a b^{\frac{3}{2}} L^{2b}; \quad (17)$$

For tangentially anisotropic components the central density vanishes, for isotropic ones it is finite and non-zero and radially anisotropic components have a central density cusp. The advantage of this family lies within the fact that most of the kinematics can be calculated analytically for positive, integer values of b (De Rijcke & Dejonghe 1998).

3.3 Determination of the dynamical mass

The only unknown in our model now is the mass M , which still acts as a free parameter. For its determination we run our models for a number of possible values, and determine the best fitting DF and the according χ^2 parameter for each value. The best fitting mass of the model is then determined as the minimum in $\chi^2(M)$.

3.4 Practical application

Practically we construct models for a sufficiently large set of masses, with a step $\Delta M = 5 \times 10^8 M_{\odot}$, 1 per cent of the input mass. For each mass we construct a DF using a library of 30 isotropic and tangential Fricke components. For computational reasons we do not include any radial components; radial models can be constructed by linear combinations of isotropic and tangential components, in which the latter have a negative weight (allowed as long as the DF remains positive over phase space). We typically used 20 components: adding more components does not significantly affect the results (neither the DF nor the mass) anymore. This is illustrated in figure 2, where we plot the χ^2 values of the various fits in function of the number of components and the value of the total mass.

A check on the fitting procedure is done by using $\beta = 0$ data, i.e. data from non-dusty Plummer models. In order to

make the test robust, we use the same strategy as De Rijcke & Dejonghe (1998): for the Plummer models that can be fitted exactly in terms of Fricke components ($q = 6, 2$ and 0), we remove these components from the library. Still, both the DF and the mass of the input models can be successfully reproduced.

In figure 3 we plot some results of the fitting procedure for the four $\beta = 2$ models. Shown are the projected light density $\rho_p(x)$, the projected dispersion $\sigma_p(x)$ and the LOSVDs at $x = 0$ kpc and $x = 10$ kpc, the innermost and outermost LOSVD in our dataset. The quality of the fit cannot be deduced from the χ^2 values, since these have no statistical meaning. At bottom row in figure 3 we show the projected fourth moment $\rho_p(x)$ of the DF, which is not included in the modelling procedure. It can be used to check the quality of the fit, which is very satisfactory in all cases.

4 RESULTS

In this section we describe the results of our fitting procedure and the kinematic properties of the models. For the sake of clarity we first explicitly define some terms.

The input models are the models that are described in section 2.1, i.e. Plummer galaxy models containing a dust component, whereas the fitted models are the models that come out of the modelling procedure, and which, by construction, contain no dust. Since each couple of parameters ($q; \beta$) corresponds to one input model, and hence one dataset and one fitted model, we will call the combination of input and fitted models corresponding to a given couple of parameters simply a model.

As the fitted models are constructed such that their projected kinematics match those of the input models, we can talk about the projected kinematics of a model. The same applies to the light profile or quantities derived from it, such as the observed luminosity L_{obs} (see section 2.2). On the contrary, when we describe spatial kinematic quantities (such as the anisotropy $\beta(r)$) or integrals thereof (such as the mass-to-light ratio), we need to distinguish between the ones corresponding to the input and fitted models, which a priori have no reason to be equal. With an apparent quantity we mean a quantity that corresponds to the fitted model, e.g. the quantity that results from the modelling procedure. With an intrinsic quantity we mean the quantity that corresponds to the input model, and hence is always independent of the optical depth. For example, all the models have the same intrinsic mass M_0 , whereas the apparent mass of the models is determined as outlined in section 3.3, and will be different for each model. Obviously, for optical depth $\tau = 0$ the apparent and intrinsic values are equal.

In this section we will compare the apparent and the intrinsic kinematic quantities of our models, as a function of the parameters β and q .

4.1 The mass and the mass-to-light ratio

In figure 4a we show the apparent dynamical mass of the models as a function of the optical depth. The global effect of the dust is clear: the mass decreases nearly linearly with the optical depth. The slope of this correlation however is strongly dependent on the orbital structure. For the very

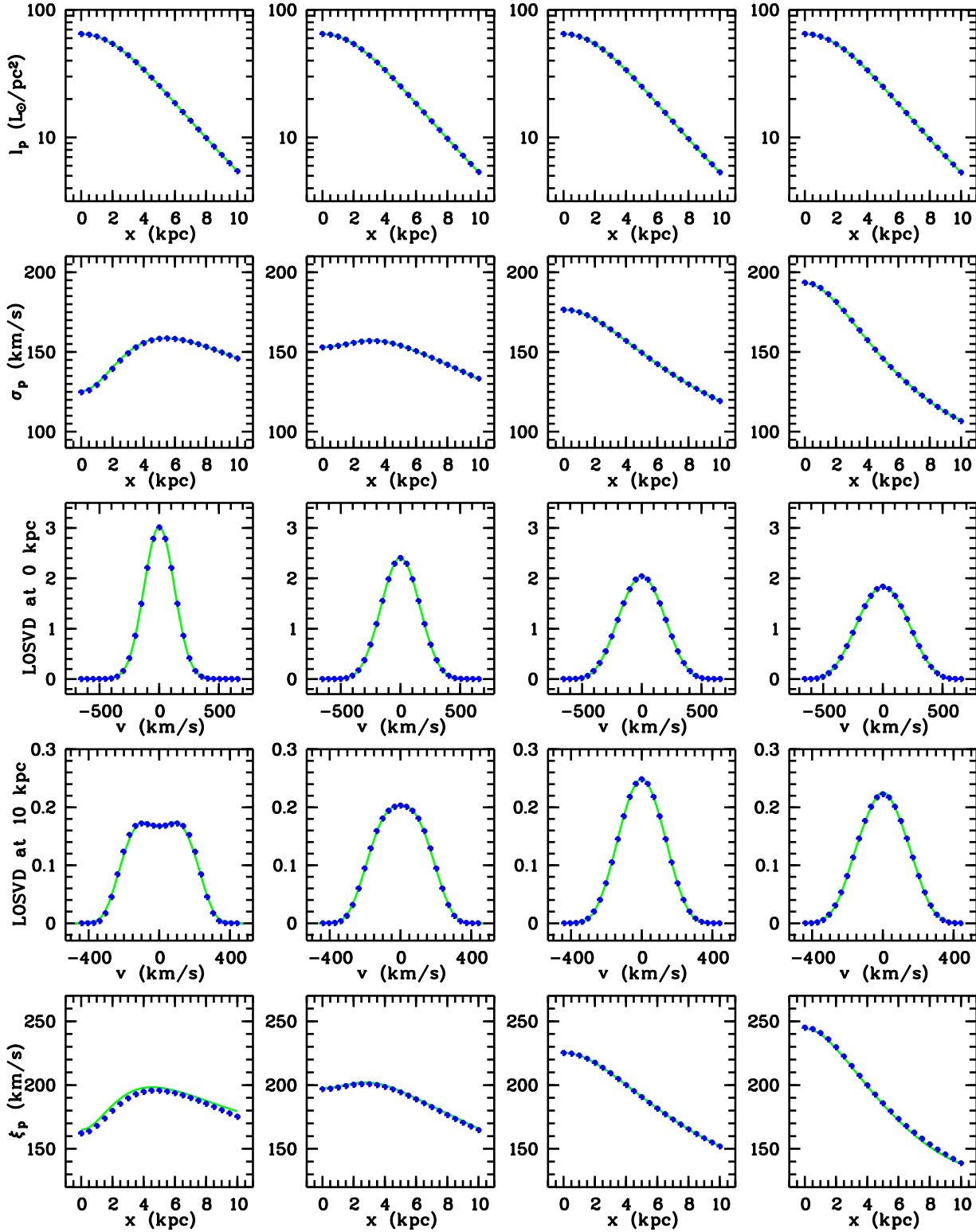


Figure 3. Results of the fitting procedure for the very tangential (left), tangential (middle left), isotropic (middle right) and radial (right) models, with optical depth $\tau = 2$. Shown are the projected light density profile $I_p(x)$ (in arbitrary units), the projected dispersion profile $\sigma_p(x)$ and the LOSVDs for $x = 0$ kpc and $x = 10$ kpc. The dots are the data points, the solid lines represent the fit. The bottom row shows the projected fourth moment $\xi_p(x)$ of the LOSVDs, which is not included in the fit and can be used as a check on the results.

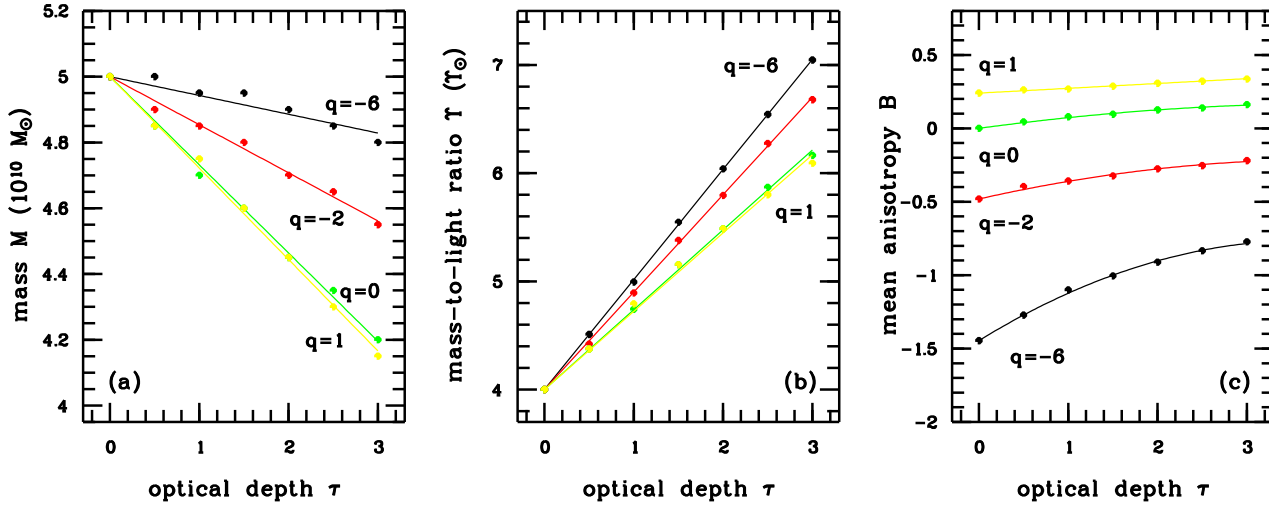


Figure 4. Three plots, showing the apparent mass M , the apparent mass-to-light ratio Υ and the apparent mean anisotropy B of our models, as a function of the optical depth τ . They are shown for different orbital structures, ranging from very tangential (black) to radial (light grey). The dots represent the results of our fits, the solid lines are least-square fits to these points, either linear (for the mass and the mass-to-light ratio) or quadratic (for the mean anisotropy). The corresponding coefficients are tabulated in table 2.

Table 2. The parameters a_M , a , a_B and b_B from the least-squares fits to M , Υ and B (see text). For a_M and a we give both the absolute and relative values.

q	a_M ($10^9 M_{\odot}$)	a (%)	a_B	b_B
-6	0.57 (1.1%)	1.02 (25%)	0.65	-0.09
-2	1.46 (3.0%)	0.90 (23%)	0.24	-0.03
0	2.68 (5.4%)	0.74 (19%)	0.12	-0.02
1	2.78 (5.6%)	0.72 (18%)	0.02	-0.00

tangential model the apparent mass is quite insensitive to the presence of dust, and the impact of the dust extinction becomes gradually stronger as we move to the tangential, the isotropic and the radial model. We fitted straight lines $M = a_M \tau$ through the data to obtain characteristic values for the mass decrease in function of the optical depth. These values are given in the second column of table 2.

The apparent luminosity of our models is calculated by integrating the apparent light density $\lambda(r)$ over space, or $\int \lambda(r) dV$ since the fitted models contain no dust (by integrating $\lambda_p(x)$ over the plane of the sky. It thus equals the observed luminosity of the dusty Plummer models, which are tabulated in the third column of table 1.

Combining these with the apparent masses we can calculate the apparent mass-to-light ratio of our models. The apparent luminosity decreases stronger than the apparent mass with increasing optical depth, such that Υ is an increasing function of τ . The dependence of Υ on the orbital structure is only determined by the apparent mass, as the apparent luminosities are independent of the orbital model. As a consequence, the dependence on q is now opposite: the mass-to-light ratio is most dramatically affected for tangential models, and the effects are smaller for radial and isotropic ones. The results are shown in figure 4b. A gain, the dependence on the optical depth is nearly linear and straight lines $\Upsilon = a \tau$ are fitted through the data points

to obtain characteristic values. These are tabulated in the third column of table 2.

4.2 The distribution function

The eight panels in figure 5 represent the isoprobability contours of eight DFs, corresponding to the four $q = 2$ models. In the upper row we plot the intrinsic DFs, whereas the lower panels represent the apparent DFs. From left to right we have, as in the previous plots, the very tangential, tangential, isotropic and radial models.

The contour plots are shown in turning point space, such that the DFs can easily be interpreted in terms of orbits. Let us first concentrate on the four upper panels. In the innermost regions of the galaxies, the shape of the DF is comparable (indeed all Plummer models are fairly isotropic in their centers). From a few kpc on however, we can clearly see how the isoprobability contours reflect the orbital structure of the model they represent. Tangential models prefer nearly circular orbits, with a small difference between apocentre and pericentre, and their contours will tend to lie alongside the diagonal axis. On the other hand, radial models prefer elongated orbits, with a large difference between apocentre and pericentre, such that their contours will tend to be more vertical. The slope of the isoprobability contours is thus indicative for the orbital structure of the model.

Let us now compare the intrinsic and apparent DFs. Concerning the central regions we see that the same structure is preserved for all orbital models. Outside this region however, there are differences, most clearly visible for the very tangential and tangential models: the contours are lying somewhat more horizontally, indicating that elongated orbits are relatively more favored. Dust obscuration thus seems to make these galaxies appear less tangential outside the innermost regions. Whether a similar trend accounts for the isotropic and radial models too, is less obvious from the

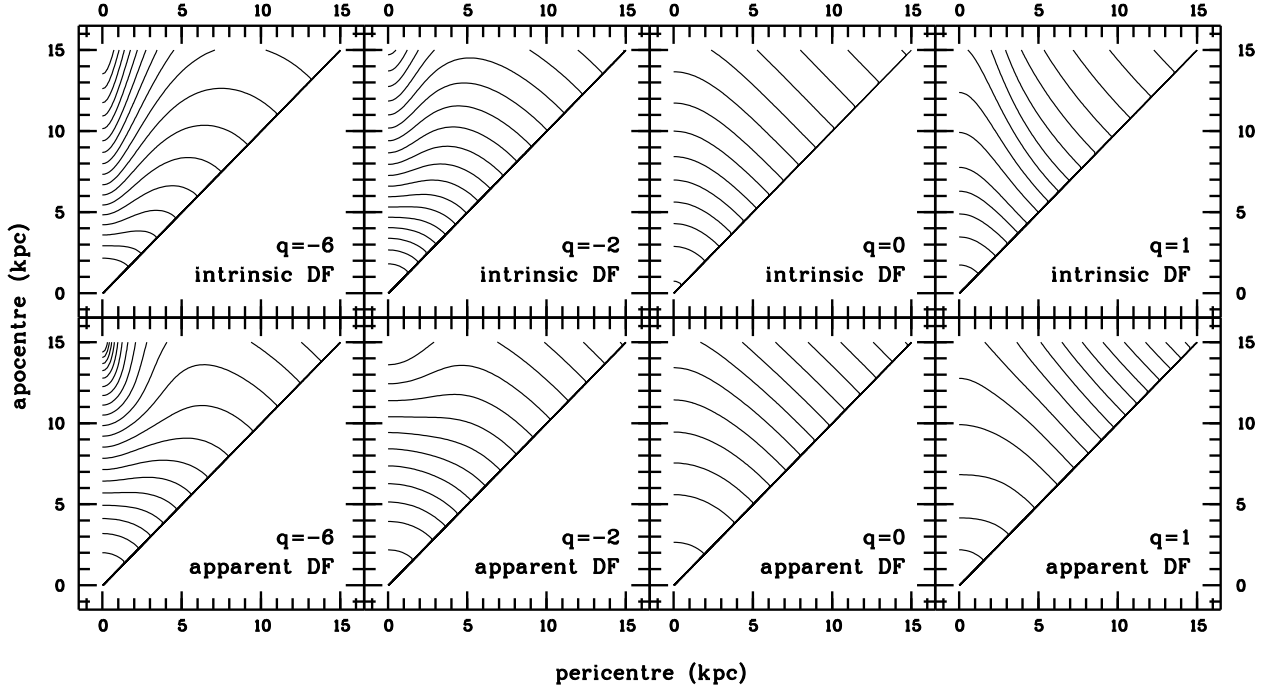


Figure 5. Isoprobability contour plots in turning point space for the $\tau = 2$ models. The upper and lower panels represent the intrinsic and the apparent DFs respectively. From left to right we have the very tangential, tangential, isotropic and radial models, as in Figure 3.

DF contour plots. Therefore we will study the anisotropy of our models in detail.

4.3 The anisotropy

The intrinsic anisotropies of our models, as defined by equation (16), can be written as

$$\langle \mu \rangle(r) = \frac{q}{2} \frac{r^2}{r^2 + c^2}; \quad (18)$$

where c represents the (true) core radius. All models are hence intrinsically isotropic in the central regions, at least if isotropy is defined only from the second order moments, and show their true orbital behavior at larger radii.

The dependence of the apparent anisotropy on the optical depth is shown, for the different orbital models, in Figure 6. Shown are apparent (solid lines) and the intrinsic (dotted lines) anisotropies of the $\tau = 1$ and $\tau = 3$ models as a function of the spatial radius. For the very tangential and tangential models, we see that the effect, as determined from the DF plots, is confirmed: as for the intrinsic orbital structure, all models are isotropic in their inner regions, and they are less tangential at larger radii. Rather logically, this effect increases with increasing optical depth. Looking at the third and fourth panel we see that also the apparent anisotropy of the isotropic and radial models increases outside a few kpc. All models thus seem to be subject to a "radialization", i.e. dust obscuration tends to make galaxies appear more radially anisotropic outside the central few kpc, even if they are already intrinsically radial.

In order to quantify the strength of the radialization in function of the input parameters q and τ , it is useful to

consider one single anisotropy parameter. We define a mean anisotropy B as

$$B = \frac{\int_0^R \langle \mu \rangle(r) r^2 dr}{\int_0^R r^2 dr} \quad (19)$$

with the integral covering the region of our fits (between 0 and 10 kpc). The intrinsic mean anisotropy for our models is of course proportional to the parameter q ; substituting (18) and (1b) in (19) we find $B = \frac{6}{25} q$.

In Figure 4c we plot the apparent mean anisotropy B for our models as a function of the optical depth. One can clearly see that B increases for increasing optical depth, and that the radialization is more dramatic the more tangential the input model. The curves in the figure are quadratic fits $B = a_B + b_B \tau^2$ to the data points, and the coefficients are tabulated in the last two columns of table 2.

5 DEPENDENCE ON THE DUST MODEL

The calculations in the previous chapters are based on a dust model whose spatial dependence is given by equation (2). But, as discussed in the introduction, very little is known about the spatial distribution of the dust in elliptical galaxies. In this chapter we will investigate whether the results so far obtained change dramatically if the relative distribution of dust and stars varies. Therefore we consider, as in paper I, a more general opacity function,

$$\langle \mu \rangle(r) = \frac{1}{\tau} = \frac{\frac{\tau}{2}}{\frac{1}{2}} \frac{1}{c} \left(1 + \frac{r^2}{c^2} \right)^{\frac{\tau}{2}} \quad (20)$$

which also satisfies the normalization condition (3), and which reduces to (2) if $\tau = 3$. The extra parameter in this

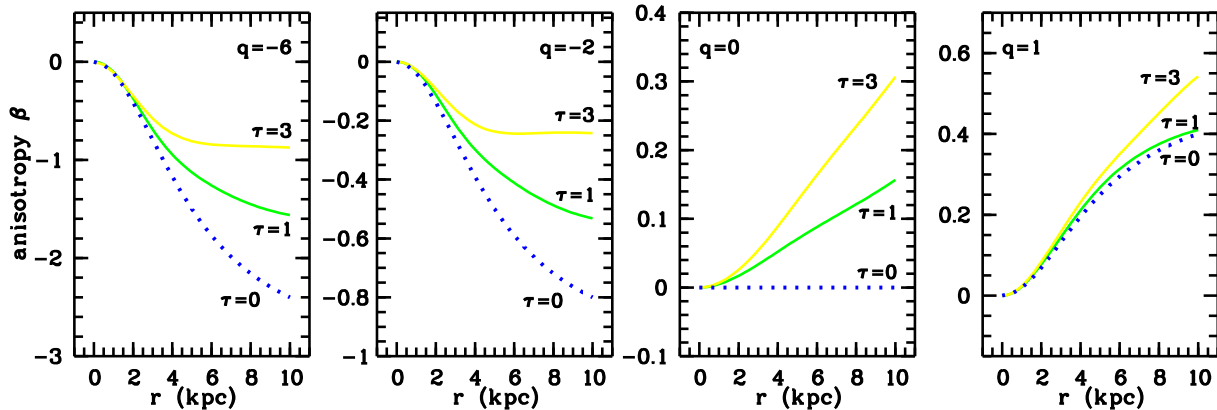


Figure 6. The orbital structure of input and output models, as characterized by the anisotropy $\beta(r)$. From left to right we have a panel with the very tangential, tangential, isotropic and radial models, as in Figure 3. The dotted lines show the intrinsic orbital structure of the input galaxies, the solid lines show the orbital structure of the $\tau = 1$ and $\tau = 3$ models.

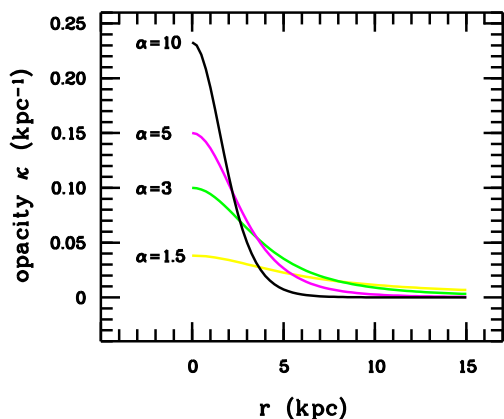


Figure 7. The opacity function $\kappa(r)$, corresponding to equation (20) for different dust exponents α . It is shown for $\tau = 1$, for other values of τ it scales linearly. For large values of α , the dust is concentrated in the central regions, for large values the distribution is extended.

family of opacity functions, the dust exponent α , sets the spatial distribution of the dust. In Figure 7 we plot the opacity function for different values of α .

Small values of α correspond to spatially extended dust distributions. The range of α is restricted to $\alpha > 1$. When α approaches this value, the dust is more or less equally distributed along the line-of-sight, and as $\alpha \rightarrow \infty$, relatively very little dust resides in the central regions of the galaxy. In the limit $\alpha \rightarrow 1$ the opacity function is such that the dust effectively forms an obscuring medium between the galaxy and the observer (see paper I), analogous to extinction of starlight due to interstellar dust in the Galaxy. This geometry is generally known as the overlying screen approximation, and it is the geometry which has, for a fixed optical depth, the largest impact on the projection of starlight. For many years the extinction in spiral galaxies was described using the cosecans law (Holmberg 1975), which implicitly assumes this geometrical distribution of stars and dust. Nowadays however, the extinction in these systems has been described using more detailed dust-stars geometries, and the

Table 3. Same as table 1, but now for a fixed optical depth $\tau = 2$ and as a function of the dust exponent α . The last row, which is labeled ND, shows the same quantities for the dust-free Plummer models.

	r_{obs} (kpc)	L_{obs} ($10^9 L_{\odot}$)	A (mag)	$\lambda_{p;0}$ (L_{\odot}/pc^2)	$v_{p;0}$ (km/s)
	1.0	5.00	4.60	1.09	178.0
	1.5	5.58	5.77	0.84	177.6
	2.0	5.91	6.75	0.67	177.1
	3.0	6.35	8.11	0.47	176.5
	5.0	6.69	9.55	0.29	176.1
ND	5.00	12.50	0.00	159.2	178.0

overlying screen model is generally considered to be unsatisfying (Bruzual, Magris & Calvet 1988; Disney, Davies & Phillips 1989; Witt, Thronson & Capuano 1992).

On the other hand, larger values of α correspond to centrally concentrated dust. For $\alpha = 5$ dust and stars have the same geometry, and if α becomes very large the extinction is confined to the central regions of the galaxy only. Silva & Wise (1996) investigated the effects of centrally concentrated dust distributions on the photometry of elliptical galaxies. They found that, for models where the stars and dust have the same spatial distribution or where the dust is more concentrated than the stars, steep color gradients would be implied in the core, even for small optical depths. However, Crane et al. (1993) and Carollo et al. (1997) imaged the cores of a set of nearby elliptical galaxies using HST, and both of them found relatively small color gradients, and hence no direct sign for the presence of centrally concentrated diffuse dust distributions.

We consider $\alpha = 1.5$, $\alpha = 2$ and $\alpha = 5$ (besides $\alpha = 3$) and create new dusty Plummer models for each of these exponents and for the four orbital modes, where we fix the optical depth at the median value $\tau = 2$. Data sets are created and these are modelled exactly as before. In particular, the observed light profile can still in a satisfying way be approximated by a Plummer potential (9), for all values of α under consideration. The observed core radii r_{obs} , as well as some other parameters of the input models, are listed in table 3 as a function of the dust exponent. In Figure 8 we

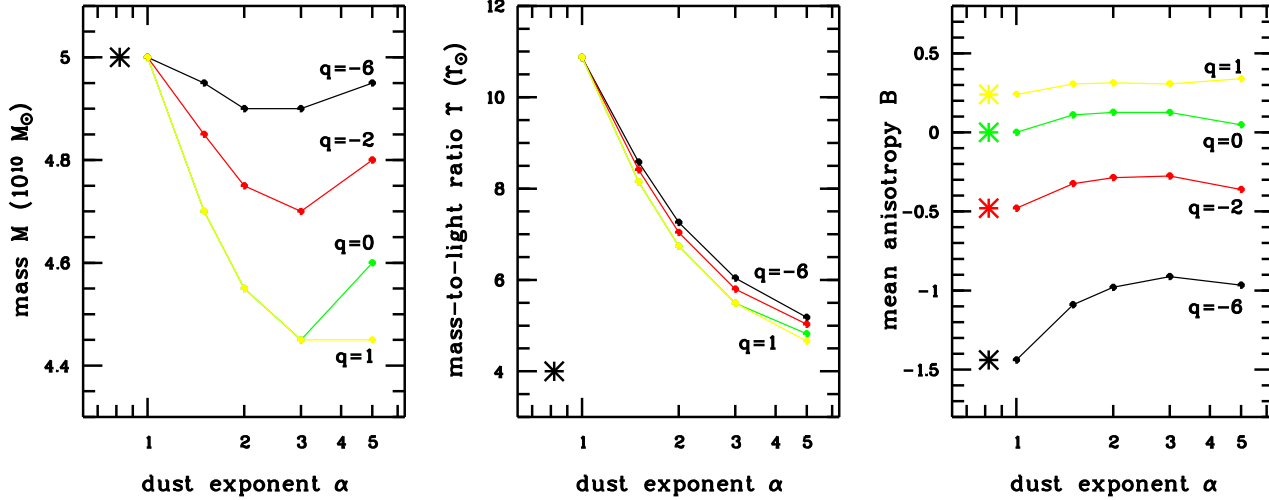


Figure 8. The apparent mass M , the apparent mass-to-light ratio Υ and the apparent mean anisotropy B , as a function of the dust exponent α , with $\beta = 2$ fixed. They are shown for the different orbital structures, ranging from very tangential (black) to radial (light grey). The dots represent the calculated values, the solid lines are just lines to guide the eye, in contrary with figure 4. The asterisks represent the intrinsic values of the represented quantities.

plot the results of our modelling: the three plots show the apparent dynamical mass M , the apparent mass-to-light ratio and the apparent mean anisotropy B as a function of the dust exponent α , for the four different values of q . The intrinsic values of these quantities are indicated by asterisks, in contrast with figure 4, where these correspond to the $\alpha = 0$ case.

Qualitatively, the effects are the same, independent of the value of the dust exponent: the apparent dynamical mass decreases, the orbital structure seems more radial and the apparent mass-to-light ratio increases. Moreover, the dependence on the orbital structure of these effects is independent of the dust exponent: the radial and isotropic models tend to lose more mass and keep their orbital structure, whereas for the tangential and very tangential models it is vice versa.

Quantitatively, there is a dependence on the dust geometry. The apparent dynamical mass and the apparent orbital structure are unaffected for both very large or very small values of α . The effects appear to be strongest for α around 3. The mass-to-light ratio however, has totally different dependence on α , it is strongly affected (a factor 2 to 3) for extended dust distributions, and the effects decrease gradually when the dust becomes centrally concentrated. In fact, Υ is largely determined by the apparent luminosity, which is a strong function of the dust geometry: the extinction is far more effective for extended than for condensed distributions (paper I, W S96).

This behavior can be illustrated when we consider the limits of very low and very high dust exponents. For an extremely extended dust distribution ($\alpha \gg 1$) on the one hand, the dust effectively forms an absorbing screen with optical depth $\tau \approx 1$ between the galaxy and the observer. Relative to the dust-free case, the light profile then decreases with a factor $\exp(-\tau/2)$, independent of the LOS, whereas the morphology of $\Sigma_p(x)$ and the shape of the LOSVDs are not affected (paper I). Hence, a model with exactly the same potential, dynamical mass and orbital structure, but with a

mass-to-light ratio which is a factor $\exp(\tau/2)$ higher, will fit these data exactly. For an extremely centrally concentrated dust distribution ($\alpha \ll 1$) on the other hand, the dust effects will be visible only in the very innermost regions. As a result, neither the projected light density, nor the LOSVDs will be severely affected, and hence the data will be nearly the same as in the dust-free model. Hence all intrinsic quantities are recovered.

The question we want to answer in this chapter was whether the results we obtained using the $\beta = 3$ model change dramatically in function of the dust geometry. As we argued, neither centrally concentrated nor very extended dust distributions seem very probable. Therefore we consider the range $2 < \alpha < 5$, where the stars are somewhat more concentrated than the dust, as representative for realistic geometries. Although M , B and Υ do vary with α in this range, the effects have qualitatively the same behavior (decreasing apparent dynamical mass, increasing apparent mean anisotropy), and quantitatively the same order of magnitude. Hence we can conclude that our results of the $\beta = 3$ case, as summarized in table 2 can be considered as representative.

6 DISCUSSION

In this paper we investigated which errors can be made by not taking dust into account in dynamical modelling procedures. Therefore we created a set of galaxy models consisting of a dust and a stellar component. We calculated the projected kinematics, taking dust into account, using the method outlined in paper I. These data sets are then modelled as if no dust were present, and the apparent dynamical properties of these models are calculated and compared to the intrinsic ones, as a function of the orbital structure of the input model, the optical depth of the dust and the dust geometry.

We find that (1) the dynamical mass of the galaxy tends

to become smaller, (2) the orbital structure seems to be radialized. For a fixed optical depth and dust geometry, the relative strength of these effects depends on the orbital structure of the input model. For radial and isotropic models the apparent mass decreases significantly, with a typical amount of 5 per cent per optical depth unit, whereas their orbital structure is hardly affected. For tangential models on the other hand, the dynamical mass is less sensitive to the presence of dust (about 3 per cent per optical depth unit for the tangential model and less for the very tangential model), whereas now the radialization is considerably stronger. Both effects are apparently coupled, in a way that reminds of the mass-anisotropy degeneration in spherical systems.

The effects are dependent on the shape of the dust distribution, but not very critically: for the dust exponents in the range $2 < \alpha < 5$ the effects are very comparable. On the one hand this is fortunate, since it means that our calculations are more or less model-independent, and can be applied for a wide range of dust geometries. On the other hand however, this means that dynamical analyses will not be able to discriminate convincingly between different values for the dust exponent. Analyses as ours can thus hardly be used to constrain the distribution (and the origin) of the smooth dust component in ellipticals. Further infrared and submillimeter observations, in particular ISO data, are necessary to solve this problem. Preliminary results include the detection of an extended, very cold dust component in the dwarf elliptical NGC 205 (Haas 1998), and of warm dust in the central regions of the Seyfert I S0 galaxy NGC 3998 (Knappe et al. 1996). A larger database of ISO imaging of early-type galaxies at both mid-infrared and far-infrared wavelengths would improve our knowledge significantly.

The combined results of paper I and this paper may at first glance seem quite contradictory. In paper I we found that the observed kinematics of elliptical galaxies are not severely affected by dust obscuration. Whence it seemed obvious that modest amounts of dust do not imply large uncertainties on dynamical mass determinations or estimates of the anisotropy of these systems. In this detailed study however we find that dust does have an important effect on the determination of the dynamical structure, in particular the dynamical mass and the anisotropy. The answer to this apparent discrepancy lies in the fact that the potential plays an important role in the determination of the internal structure of galaxies. Dejonghe & Merritt (1992) show that, in case of a spherical two-integral system, the knowledge of the potential and the entire set of LOSVDs suffice to determine the DF uniquely. The potential itself can be considerably constrained by the LOSVDs, but is not uniquely determined, such that a set of potentials will usually yield acceptable models for a data set. Often one chooses that potential that is derived from the observed light profile, if this one is one of the possible choices (e.g. if dark matter is not assumed to play a major role). But if dust is present, the light profile will be severely affected, even by small amounts of dust, such that the matching potential will not be the correct one. And as dust is assumed to be present in a major fraction of the early-type galaxies, we argue that it is important to at least be aware of its effects, which may not be as trivial as one might imagine. As SW S96 stressed, all broadband observations of elliptical galaxies may be affected by dust, and hence dust should be seriously taken into

account in their interpretation. We now can add that dust does also play a role in dynamical analyses, and hence that it should also here be taken into account, in a non-trivial way.

We close by giving a simple example to illustrate this point. A simple way to estimate the mass of a gravitating system is its virial mass. For example, Tonry & Davis (1981) estimate the masses for a set of 373 elliptical galaxies using a relation where mass is proportional to the effective radius and the square of the central dispersion. Although it is nowadays possible to obtain much better mass estimates for nearby galaxies, the virial mass estimate is still one of the only tools to constrain the mass of galaxies and clusters at intermediate or high redshifts (Carlberg et al. 1996, Carlberg, Yee & Ellingson 1997, Tran et al. 1999). The question is now how to correct these mass estimates for the presence of dust? A straightforward way is to estimate an amount of dust using IRAS or ISO data, and calculate the effects on dispersion and scale length. Dispersions are only slightly affected by dust absorption (paper I), whereas scale lengths as the effective radius or the core radius can increase substantially, as dust primarily removes light from the centre of the system. Hence we find that the apparent mass of the galaxy would increase as a function of α , while we find, using detailed kinematic modelling, that the apparent mass decreases with increasing optical depth. Moreover, this correction will be independent of the orbital structure of the model. This again illustrates the fact that dust effects are non-trivial and should be fully taken into account.

REFERENCES

- Baes M., Dejonghe H., 2000, MNRAS, 313, 153 [paper I]
 Begum A.J.N., Hogg D.E., Roberts M.S., 1992, ApJ, 387, 484
 Buzuladze A., Magris G.C., Calvet N., 1988, ApJ, 333, 673
 Carlberg R.G., Yee H.K.C., Ellingson E., Abraham R., Gavel
 P., Morris S., Pritchet C.J., 1996, ApJ, 462, 32
 Carlberg R.G., Yee H.K.C., Ellingson E., 1997, ApJ, 478, 462
 Carollo C.M., Franx M., Illingworth G.D., Forbes D.A., 1997,
 ApJ, 481, 710
 Crane P., Stiavelli M., King I.R., Deharveng J.M., Albrecht
 R., Barbieri C., Blades J.C., Boksenberg A., Disney M.J.,
 Jakobsen P., Kamperman T.M., Machtetto F., Mackay C.D.,
 Paresce F., Weigelt G., Baxter D., Greeneld P., Jedrzejewski
 R., Nota A., Sparks W.B., 1993, AJ, 106, 1371
 de Jong T., Nørgaard-Nielsen H.U., Hansen L., Jørgensen H.E.,
 1990, A & A, 232, 317
 Dejonghe H., 1986, Phys. Rep., 133, 225
 Dejonghe H., 1987, MNRAS, 224, 13
 Dejonghe H., 1989, ApJ, 343, 113

? There is still no clarity about the amount and the sources of dust grains in the intergalactic medium of galaxy clusters. Studies investigating the extinction effects of background galaxies and quasars yield controversial results (Ferguson 1993, Maoz 1995). Also the FIR emission is still inconclusive: recently, extended ISO emission has been interpreted as evidence for the presence of intracluster dust in the Coma cluster (Stickel et al. 1998) and Abell 2670 (Hansen et al. 1999), but this evidence is still controversial (Quillen et al. 1999). The presence of intergalactic dust still isn't firmly established, and, as Popescu et al. (2000) suggest, the new generation of submillimeter interferometers might contribute significantly to solve this problem.

- Dejonghe H., Merritt D., 1992, *ApJ*, 391, 531
 De Rijcke S., Dejonghe H., 1998, *MNRAS*, 298, 677
 Disney M.J., Davies J.I., Phillips S., 1989, *MNRAS*, 239, 939
 Ebnetter K., Balick B., 1985, *AJ*, 90, 183
 Fabian A.C., Nulsen P.E.J., Canizares C.R., 1991, *A&AR*, 2, 191
 Ferguson H.C., 1993, *MNRAS*, 263, 343
 Fich M., Hodge P., 1991, *ApJL*, 374, L17
 Fich M., Hodge P., 1993, *ApJ*, 415, 75
 Forbes D.A., 1991, *MNRAS*, 249, 779
 Gerhard O.E., 1993, *MNRAS*, 265, 213
 Goudfrooij P., de Jong T., 1995, *A&A*, 298, 784 [GdJ95]
 Haas M., 1998, *A&A*, 337, L1
 Hansen L., Jørgensen H.E., Nørgaard-Nielsen H.U., 1995, *A&A*, 297, 13
 Hansen L., Jørgensen H.E., Nørgaard-Nielsen H.U., Pedersen K., Goudfrooij P., Linden-Vornle M.J.D., 1999, *A&A*, 349, 406
 Holmberg E., 1975, *Stars and Stellar Systems IX*, University of Chicago, 123
 Knapp G.R., Guhathakurta P., Kim D.-W., Jura M., 1989, *ApJS*, 70, 329
 Knapp G.R., Gunn J.E., Wynn-Williams C.G., 1992, *ApJ*, 399, 76
 Knapp G.R., Rupen M.P., Fich M., Harper D.A., Wynn-Williams C.G., 1996, *A&A*, 315, L75
 Kwan J., Xie S., 1992, *ApJ*, 398, 105
 Maoz D., 1995, *ApJ*, 455, L115
 Merluzzi P., 1998, *A&A*, 338, 807
 Mollenhofs C., Arenbach G., 1986, *A&A*, 154, 219
 Popescu C.C., Turs R.J., Fischera J., Volk H., 2000, *astro-ph/0001053*, accepted for publication in *A&A*
 Quillen A.C., Rieke G.H., Rieke M.J., Caldwell N., Engelbracht C.W., 1999, *ApJ*, 518, 632
 Roberts M.S., Hogg D.E., Bregman J.N., Forman W.R., Jones C., 1991, *ApJS*, 75, 751
 Silva D.R., Wise M.S., 1996, *ApJ*, 457, L71
 Sparks W.B., Macchetto F., Golombek D., 1989, *ApJ*, 217, 425
 Stickel M., Lemke D., Mattila K., Haikala L.K., Haas M., 1998, *A&A*, 329, 55
 Tonry J.L., Davis M., 1981, *ApJ*, 246, 666
 Tran K.-V.H., Kelson D.D., van Dokkum P., Franx M., Illingworth G.D., Magee D., 1999, *ApJ*, 522, 39
 Tsai J.C., Mathews W.G., 1996, *ApJ*, 468, 571
 van der Marel R.P., Franx M., 1993, *ApJ*, 407, 525
 van Dokkum P.G., Franx M., 1995, *AJ*, 110, 2027
 Veron-Cetty M.-P., Veron P., 1988, *A&A*, 204, 28
 Wiklund T., Henkel C., 1995, *A&A*, 297, L71
 Wise M.W., Silva D.R., 1996, *ApJ*, 461, 155 [W S96]
 Wise M.W., Silva D.R., 1997, in *The Nature of Elliptical Galaxies*, Proceedings of the Second Stromlo Symposium, eds. M. Amaldi, G.S. Da Costa & P. Saha, *ASP Conference Series*, vol. 116, p. 364
 Witt A.N., Thronson H.A. Jr., Capuano J.M. Jr., 1992, *ApJ*, 393, 611

This paper has been produced using the Royal Astronomical Society/Baskwell Science L^AT_EX style file.